Absorption-Based Hyperspectral Imaging and Analysis of Single Erythrocytes

Ji Youn Lee, Matthew L. Clarke, Fuyuki Tokumasu, John F. Lesoine, David W. Allen, Robert Chang, Maritoni Litorja, and Jeeseong Hwang

(Invited Paper)

***Abstract*—We report an absorption-based hyperspectral imaging and analysis technique to resolve unique physicochemical characteristics of subcellular substances in single erythrocytes. We constructed a microscope system installed with a spectral light engine capable of controlling the spectral shape of the illumination light by a digital micromirror device. The hyperspectral imaging system and the sequential maximum angle convex cone algorithm allow us to extract unique spectral signatures (i.e., endmembers) for different types of hemoglobin, such as oxyhemoglobin, methemoglobin, and hemozoin, and scatter from cell membrane in single erythrocytes. Further statistical endmember analysis, conducted on the hyperspectral image data, provides the abundances of specific endmembers, which can be used to build intracellular maps of the distribution of substances of interest. In addition, we perform modeling based on Mie theory to explain the scattering signatures as a function of scattering angle. The developed imaging and analysis technique enables label-free molecular imaging of endogenous biomarkers in single erythrocytes in order to build oxymetric standards on a cellular level and ultimately for *in vivo* as well.**

***Index Terms*—Absorption spectra of hemoglobin, endmember analysis, erythrocyte (red blood cell), hyperspectral imaging, label-free molecular imaging, scattering signature, sequential maximum angle convex cone (SMACC) algorithm, spectral light engine.**

I. Introduction

HYPERSPECTRAL imaging effectively employs broadband illumination and/or spectroscopic detection of photons after their interaction with specimens. Hyperspectral imaging can be performed on varying levels of dimensional complexity. The most common approach consists of spatial coordinates (x, y) with a third coordinate in the spectral domain λ. The latter is generalized to refer to wavelengths at which either specimens are interrogated (e.g., $\lambda_{\mathrm{excitation}}$) or post-interrogating signals are analyzed (e.g., $\lambda_{\mathrm{emission}}$). Higher order dimensional dataset or "cubes" can be constructed by adding additional dimensions, such as the z-axis for confocal fluorescence microscopy, and other spectral dimensions (e.g., $\lambda_{\mathrm{excitation}}$, $\lambda_{\mathrm{emission}}$, $\lambda_{\mathrm{transmission}}$, $\lambda_{\mathrm{scattering}}$). Hyperspectral imaging has been used in many biological and biomedical applications using bioluminescence or fluorescence, both *in vitro* and *in vivo* [1]–[6]. For instance, in fluorescence microscopy, spectral tuning of the optical components, such as excitation and emission filters and detectors, is necessary to enhance signals against background autofluorescence [7] or against other fluorophores to minimize the spectral overlap in the signal [8]. Recently, hyperspectral imaging of endogenous biomarkers has been of increasing interest for a variety of applications. Examples include label-free imaging of chemical species in cells and tissues [9], [10], optical spectroscopic biopsy of diseases [11], and real-time *in vivo* monitoring of oxygenation states of tissues and organs under a surgical procedure [12], [13]. However, previous approaches have been limited either to fluorescence-based systems or to macroscopic measurements. In this paper, we construct a wide-field hyperspectral microscope and perform absorption-based hyperspectral imaging on single cells using endogenous chromophores.

Erythrocytes or red blood cells are the most common type of cells in the blood, and they are the principal oxygen carriers to body tissues. Erythrocytes contain high concentrations of cytoplasmic hemoglobin (Hb), prominent solute and ion transport systems, and deformable submembrane cytoskeleton networks, allowing for the delivery of oxygen to tissues, and survive repeated passage through capillaries. Hb is an iron-containing oxygen-carrying protein present in erythrocytes of all vertebrates and in the tissues of some invertebrates. Hb in the pulmonary vein is in an oxygenated state and transports oxygen from lungs or gills to the tissues in the body. Oxyhemoglobin (oxyHb) releases oxygen to the tissues to be converted to deoxyhemoglobin (deoxyHb) which collects carbon dioxide to be exchanged with oxygen from the air or water. The absorption spectra of oxyHb and deoxyHb are different and, therefore, have been used as indicators to assess oxygenated states of tissues and organs [2], [14]. OxyHb can be converted to methemoglobin (metHb) after interactions with water molecules by releasing superoxide as a by-product [15]. The iron in heme group of metHb is in the ferric (Fe^{3+}) state while that in oxyHb is in the ferrous (Fe^{2+}) state. MetHb is not capable of carrying oxygen and has a different absorption spectrum from that of oxyHb. In normal

Manuscript received June 14, 2011; revised July 25, 2011; accepted July 25, 2011. Date of publication August 12, 2011; date of current version June 1, 2012. This work was supported by the NIST Innovations in Measurement Science Program on Optical Medical Imaging and by the Intramural Research Program of the NIAID, NIH. J. Y. Lee and M. L. Clarke contributed equally to this work.

J. Y. Lee, M. L. Clarke, J. F. Lesoine, D. W. Allen, R. Chang, M. Litorja, and J. Hwang are with the Optical Technology Division, National Institute of Standards and Technology, Gaithersburg, MD 20899-8443 (e-mail: jiyoun.lee@nist.gov; matthew.clarke@nist.gov; john.lesoine@nist.gov; david.allen@nist.gov; robert.chang@nist.gov; maritoni.litorja@nist.gov; jch@nist.gov).

F. Tokumasu is with the Laboratory of Malaria and Vector Research, National Institutes of Health, Bethesda, MD 20892 (e-mail: ftokumasu@niaid.nih.gov).

Color versions of one or more of the figures in this paper are available online at http://ieeexplore.ieee.org.

Digital Object Identifier 10.1109/JSTQE.2011.2164239

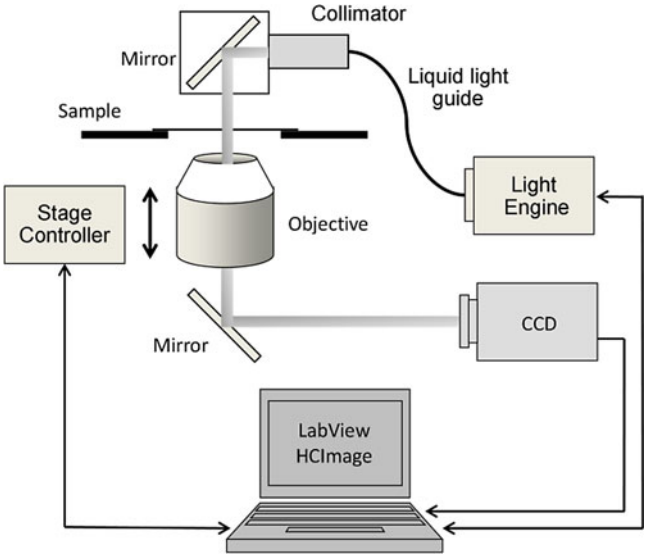

Fig. 1. Schematic of the hyperspectral transmittance microscope.

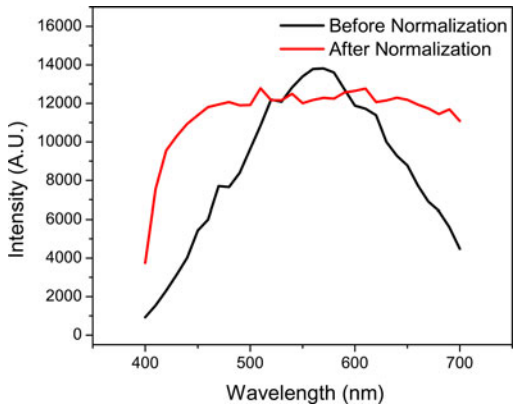

Fig. 2. Comparison of the spectrally dependent excitation intensity as a function of wavelength before and after the adjustment of the excitation light intensity by adjusting DMD arrays. The adjustment effectively normalized the light intensity between 450 and 700 nm.

human blood, 1–2% of Hb exists in the form of metHb and the reduction of metHb depends on the reduced diphosphopyridine nucleotide-dehydrogenase reduction system [16]. A higher percentage is found in individuals suffering methemoglobinemia caused by a genetic disorder or exposure to certain chemicals.

Another form of Hb analyzed in this study is hemozoin found in human erythrocytes infected by malaria parasites which consume Hbs as a major nutrient source. Digestion of Hb releases toxic-free heme (α-hematin, ferriprotoporphyrin IX) which can be polymerized into β-hematin in the form of insoluble microcrystalline material called hemozoin or malaria pigment [17]–[19]. The molecule consists of an unusual polymer of hemes linked between the central ferric ion of one heme and a carboxylate side-group oxygen of another. The hemes are sequestered via this linkage into an insoluble product, providing a unique way for the malaria parasite to detoxify the free heme. The spectral signatures of the hemozoin have been studied by Fourier transform infrared [19] and Raman spectroscopy [20], [21].

In this study, we demonstrate that our absorption-based hyperspectral imaging system can spectrally resolve different types of Hb in single erythrocytes. The hyperspectral microscope system collects transmittance intensities of erythrocytes in the $(x, y, \lambda_{\mathrm{illumination}})$ 3-D data cube format. Then, we normalize the intensities with a blank signal and convert the data cube to have absorption intensities. A data analysis algorithm based on spectral angle measurement extracts endmembers of unique spectral signatures of different types of Hbs and other features in single cells [22], [23]. In addition, a simple Mie scattering model is considered to correct for attenuation due to wavelength-dependent scattering effects.

II. Methods

A. Hyperspectral Microscope Setup

The hyperspectral microscope setup, schematically shown in Fig. 1, was constructed using a Zeiss Axiovert 100 inverted microscope.[1] Details of design and analysis of the hyperspectral microscope have been published elsewhere [24]. In brief, a tunable light engine (OL490, Gooch and Housego, Orlando, FL) was coupled to the microscope via a liquid light guide and collimator. The collimator was attached in place of the bright field or arc lamp housing. The objective focus was adjusted by an MS-2000 stage controller (Applied Scientific Controller, Eugene, OR). In contrast to previous work [24], the results presented in this paper were collected solely with a Zeiss 63× achroplan objective lens in transmission mode. This objective exhibits negligible changes (∼20 nm) in the focal position as a function of the illumination wavelength (380–780 nm), eliminating the need for chromatic aberration correction in the z-axis during data collection.

A Hamamatsu ORCA2 charge coupled device (CCD) (Hamamatsu Corporation, Japan) camera was used to collect (x, y) transmission images at a wavelength ($\lambda_{\mathrm{illumination}}$) tuned by the light engine. The dynamic range of each image pixel of the CCD camera was 16 bit with zero gain. For cell imaging, a sequence of 61 images were collected corresponding to wavelength segments of 5 nm from 400 to 700 nm. All instruments were synchronized using a LabVIEW program (National Instruments, Austin, TX), with the camera controlled via HCImage (Hamamatsu Corporation, Japan). The bandwidth of the illumination wavelength was experimentally determined to be approximately 10 nm [24]. The transmittance spectral profile of the spectral light engine through a blank cover slip was initially measured by the ORCA2 camera and is shown in Fig. 2. Since the light source, optics, and camera all exhibit spectrally dependent properties (e.g., power, transmission, and sensitivity), a reference hyperspectral data cube was used to normalize the intensity profile of the detected signal. This normalization provides constant illumination intensity from 450 to 700 nm, expanding the dynamic range in the measurement of absorption

[1]Certain commercial equipment, instruments, or materials are identified in this paper. Such identification does not imply recommendation or endorsement by the National Institute of Standards and Technology, nor does it imply that the materials or equipment identified are necessarily the best available for the purpose.

coefficient of specimens in this wavelength range. The normalized spectral profile was used to calculate the absorption spectra of single cells.

The transmittance T_λ and the absorbance A_λ at each wavelength are calculated by the following equations:

$$T_\lambda = \frac{I - I_{\mathrm{dark}}}{I_0} \tag{1}$$

$$A_\lambda = -\log(T_\lambda) \tag{2}$$

where I_0 is the intensity of the incident light from the spectral light engine, I is the intensity of the light collected by the objective, and I_{dark} is the intensity of the stray light collected by the objective.

B. Image Correction Processing to Remove Background Signal From the Light Engine

The spectral profile of the illuminating light was controlled by a digital micromirror device (DMD) array chip onto which spectrally dispersed light was projected. A DMD chip consisted of 1024 × 768 microscopic mirrors. The mirrors were individually addressable and rotate ±10° (i.e., total rotational angle of 20°) to "ON" or "OFF" state. In the ON state, the light was reflected into the lens, and consequently, the corresponding pixel contributed in illuminating the sample. In the mirror array, each column corresponds to a narrow spectral bandwidth, and the number of "ON" mirrors within this column determines the intensity of that specific bandwidth. Ideally, in the OFF state, the light is entirely directed away from the sample into a light trap. However, in reality, there existed a nonnegligible amount of stray light in the OFF state due to the reflection by mirrors and other areas of the chip. Therefore, we acquired "dark" noise images to subtract the background stray light from the original images and, therefore, to correct the dataset both spatially and spectrally. A dark noise image was collected with all the mirrors in the "OFF" position. The corrected hyperspectral dataset was further processed and analyzed using MATLAB (MathWorks, Natick, MA), ImageJ, and ENVI (ITT Visual Information Solution, Boulder, CO).

C. Preparation of Hb Solutions and Erythrocytes

A Hb solution was prepared by dissolving human-derived ferrous-stabilized Hb A_0 (Sigma-Aldrich, St. Louis, MO) in 1× phosphate-buffered saline at a concentration of 2 mg/mL. For oxidization of the Hb solution, sodium nitrite ($NaNO_2$) was added to make a final concentration of 100 mM and incubated for 30 min at 37 °C.

For the preparation of erythrocytes, O+ blood was purchased from The Interstate Blood Bank and processed using Sepa-cell R-500 leukocyte-reduction filter (Baxter, Deerfield, IL). Erythrocytes were washed three times with RPMI1640 base media (Invitrogen, Carlsbad, CA) and stored at 4 °C until used. *Plasmodium falciparum* (*Pf*) 3D7 line parasites were grown in RPMI1640 media containing 25 mM HEPES pH.7.4 (Carbochem, EMD Chemicals, Inc. Gibbstown, NJ), 2 mg/mL sodium carbonate (Invitrogen, Carlsbad, CA), 0.1 mM hypoxanthine (Sigma-Aldrich, St. Louis, MO), 10 mg/L Gentamicin (Invitrogen, Carlsbad, CA), and 5 mg/L Albumax II (Invitrogen, Carlsbad, CA) at 5% hematocrit at 37 °C in a 5% O_2, 5% CO_2, 90% N_2 atmosphere. The culture with matured trophozoite stage parasites was applied onto clean coverglasses (18 × 18 mm, #1.5, Thomas Scientific, Swedesboro, NJ) coated with collagen (Chrono-PAR, Chrono-log, Havertown, PA) and fixed with 13.5 mg/mL dimethylsuberimidate (Sigma-Aldrich, St. Louis, MO) in a 38.1 mg/mL sodium borate buffer containing 0.2 mg/mL $MgCl_2$ using an established methods [25]. To accelerate Hb degradation from normal Hb to metHb, we treated erythrocytes with 1 mM $NaNO_2$ in HEPES buffered serine for 30 min at 37 °C [26]. After treatment, erythrocytes were washed three times with HEPES and resuspended in RPMI1640 media.

D. Extraction of Spectral Endmembers From Hyperspectral Cubes

In principle, a spectrum of multicomponent scene can be described as a linear superposition of spectra of "pure" individual substances called "endmember." In this study, the absorption spectrum of a chemical component present in cells is an endmember. In the presence of scattering, additional endmember may be required to consider the wavelength-dependent scattering contribution to measured transmission spectra. Here, we extracted endmembers from hyperspectral dataset collected from erythrocytes under different conditions. The endmember spectra were then used as the reference spectra in measuring the abundance of substances spatially in unknown scenes. The main substances of interest in this study include oxyHb, metHb, and hemozoin. The spectra of those substances are accompanied by the inherent scatter and background.

The images for this study were evaluated using the sequential maximum angle convex cone (SMACC) algorithm using ENVI image analysis software [22], [23]. SMACC extracts the endmembers from the data cube without *a priori* knowledge of absorption spectra of the pure substances. It searches for extreme vectors, those that cannot be derived by a positive linear combination of other vectors, sequentially. Each additional extreme vector is selected by searching for the vector with the greatest angle from the cone formed by the other selected vectors. For each extreme vector which is identified as an endmember, a grayscale abundance image is generated. The abundance image shows the spatial relationship of the proportion of a given endmember on a pixel-by-pixel basis.

The parameters for the SMACC analysis were selected to return up to N endmembers ($N = 3$, 4, or 5 depending on the sample), positive only by coalescing redundant endmembers at a spectral angle mapper (SAM) coalesce value of 0.15 radians. From this, a set of N eigenspectra and corresponding abundance images were obtained. These eigenspectra were then recombined as a linear combination in proportion to the grayscale abundance images, resulting in a product that spectrally resembles the original data cube. The net result is a data cube which is intended to have the same level of spatial and spectral complexity as the original.

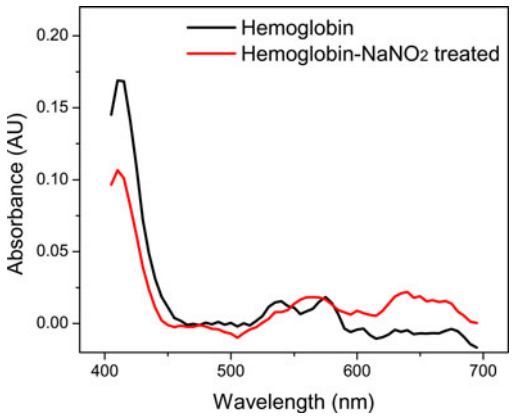

Fig. 3. Change in absorption spectra of Hb solution after treatment with $NaNO_2$. The adjacent two characteristic peaks at 545 nm and 575 nm in Hb solution disappeared after treatment. Also, the large peak at 415 nm slightly blue-shifted after treatment. These spectral changes suggest that oxyHb is converted to metHb by the oxidizing agent, $NaNO_2$.

III. Results and Discussions

A. Absorption Spectra and Abundance Maps for OxyHb and metHb in Erythrocytes

Prior to the analysis of single-cell images, we measured hyperspectral data cubes from bulk Hb solutions, either in the absence or in the presence of an oxidizing agent $NaNO_2$. Absorption spectra of the Hb solutions are shown in Fig. 3. The spectrum of the Hb solution shows three characteristic peaks of the oxyHb at 415, 545, and 575 nm. Upon the addition of $NaNO_2$ to the Hb solution, the characteristic peaks of the oxyHb between 525 and 575 nm disappeared. In addition, the peak observed at 415 nm in the Hb solution shifted to a lower wavelength and absorption at 630 nm increased significantly [15]. These spectrum changes are unique characteristics of the metHb where the oxygen molecules were effectively removed from Hb, as $NaNO_2$ transformed the iron in the heme group from a ferrous (Fe^{2+}) state to a nonoxygen-binding ferric (Fe^{3+}) state.

A hyperspectral data cube of erythrocytes treated with $NaNO_2$ was analyzed to directly obtain endmembers of oxyHb and metHb. Fig. 4(a) shows an averaged image over the entire data cube of the hyperspectral images achieved as the wavelength of the transmission light is varied from 400 to 700 nm in 5 nm increments. Upon treatment of the erythrocytes with $NaNO_2$, they developed small protruded round features as shown in Fig. 4(a). The morphological change in cell membrane was possibly in response to a hypertonic environment of $NaNO_2$ in the buffer.

The treatment with $NaNO_2$ for a relatively short period of time resulted in partial conversion of oxyHb to metHb, so we could obtain mixed population of cells whose major form of Hb is either oxyHb or metHb. We chose a pixel within 11 different cells [numbered 1 to 11 in Fig. 4(a)] and analyzed their spectral profiles. The profiles were classified into two absorption spectra windows. Pixels chosen within cells from 1 to 6 showed a typical oxyHb spectrum with two local maxima at 545 and 575 nm [black lines in Fig. 4(b)] while the others showed a typical metHb spectrum without them [red lines in Fig. 4(b)]. Two reference spectra for oxyHb [#2 in Fig. 4(b)] and metHb [#7 in Fig. 4(b)] were selected from these absorption spectra, and SAM analyses were conducted to find the pixels matching each reference spectrum, and the results are shown in Fig. 4(c)–(h). SAM compares every pixel in the scene to a reference spectrum. The reference spectrum and each unknown pixel spectrum are considered as vectors and the angle between the two is determined. A smaller value for an SAM result corresponds to a smaller angle between the vectors and also a closer match. Since it is the angle between the vectors being evaluated, this method is not sensitive to variations in brightness. For the graphical representation in this paper, the darker color represents a closer match between the reference and the unknown pixel.

The eigenstate abundance maps of oxyHb and metHb over the entire spectral range of the measurement demonstrated cell-to-cell variation as shown in Fig. 4(c) and (d), respectively. These images also show that the abundance of each eigenstate was reversed when the same cells are compared. This result qualitatively confirmed that the conversion from oxyHb to metHb was underway. Interestingly, the reversal of the abundance appeared to be more significant as the algorithm was applied only for wavelengths 400–450 nm [see Fig. 4(e) and (f)], where the metHb spectra were expected to show a blue-shift. This implied that the peak shift in this wavelength range was a stronger indicator to differentiate the eigenstate of metHb from that of oxyHb. However, limiting the analysis within this wavelength region can also be unfavorable because the abundance map contains a strong forward-scattering signal at shorter wavelengths, resulting in a strong signal around the edge of cells and any topographic feature. Fig. 4(g) and (h) demonstrates that these forward-scattering signals stand out in the cells where the eigenstate abundance signals become comparable to or weaker than the forward-scattering signal. In this paper, forward-scattering contributions are addressed further with a simulation in a subsequent section.

B. Endmember Extraction From Uninfected and Pf-Infected Erythrocytes: oxyHb, Hemozoin, and Membrane Scattering

Our initial study on $NaNO_2$ treated erythrocytes provided a potential platform for generalized measurements and analyses for erythrocytes containing more complex characteristic eigenstates. To this end, *Pf*-infected erythrocytes were prepared and mixed with uninfected erythrocytes to demonstrate the capability of separating infected erythrocytes from uninfected erythrocytes by hyperspectral imaging and analysis. With *a priori* information on the regions of interest either in uninfected or in infected erythrocytes, three characteristic eigenstate endmembers were extracted from the (x, y, λ) dataset corresponding to each region. Uninfected erythrocytes have biconcave shape and contain no special feature while infected erythrocytes lose their biconcave shape and contain hemozoin formed from Hb consumption and heme biocrystallization by parasites. The absorption spectra extracted from the dark region [blue in Fig. 5(b)] of the *Pf*-infected erythrocyte were in good agreement with the results on isolated *Pf*-produced hemozoin spectra reported elsewhere [27], validating the endmember extraction algorithm in

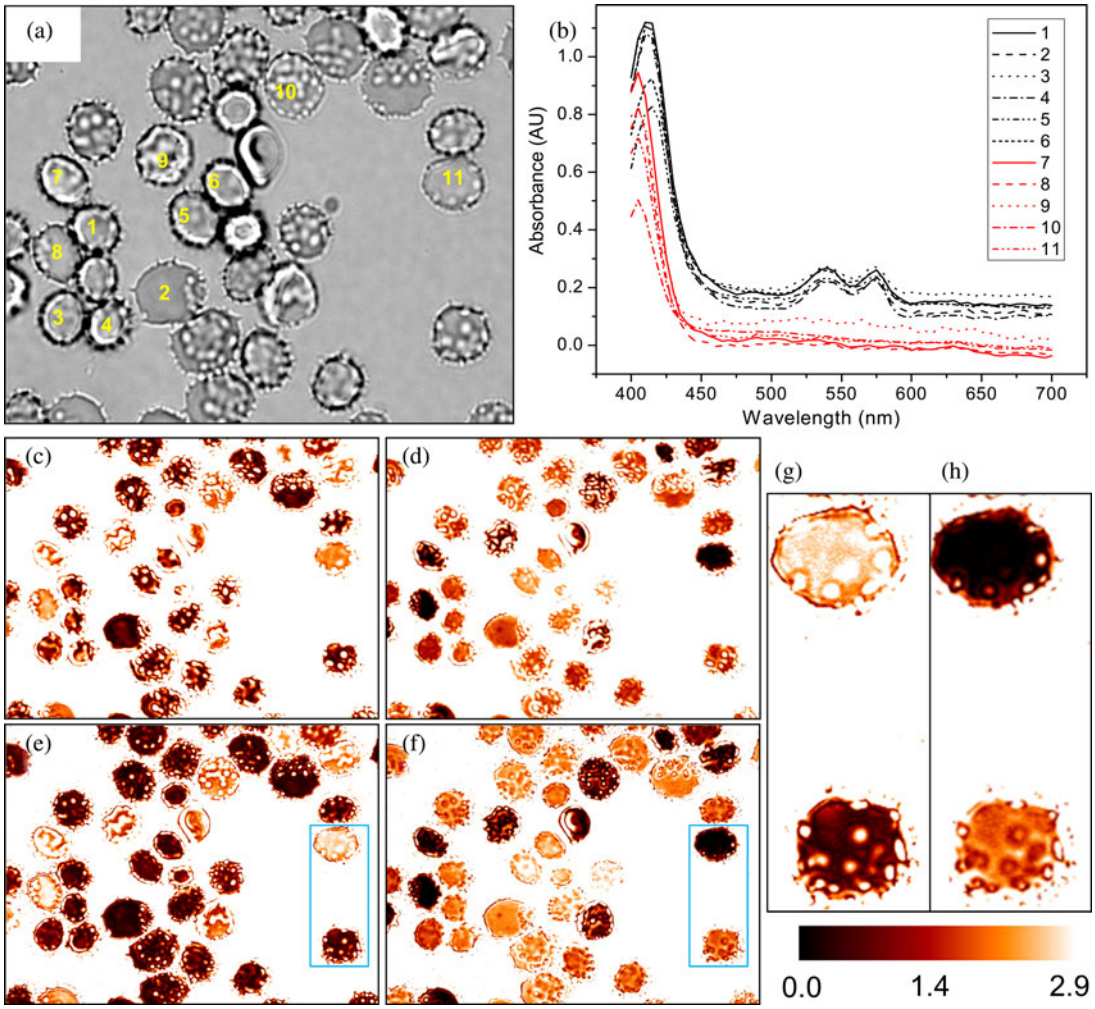

Fig. 4. (a) Averaged intensity map calculated from all the absorption spectra of erythrocytes treated with $NaNO_2$. (b) Absorption spectral profiles from randomly selected pixels within the cells. Each number corresponds to the pixel position in the image. The local maxima between 525 nm and 580 nm, which appear in cells 1 to 6, are unique characteristics of oxyHb. Absorption spectra in cells 7 to 11 do not show those maxima. These spectra were plotted by y-axis offset of 0.2 unit in the absorbance value. (c) and (d) Spectral angle maps were calculated by the extracted spectra of #2 (for C) and #7 (for D), respectively, for the entire wavelength range. (e) and (f) Spectral angle maps were calculated by applying the extracted spectra of #2 (for E) and #7 (for F), respectively, for the wavelength range of 400 to 700 nm. (g) and (h) Magnified views of the enclosed regions of (e) and (f), respectively.

this study. In addition, the absorption spectra extracted from a region [red in Fig. 5(c)] of uninfected erythrocytes rich in oxyHb exhibited typical absorption spectra of oxyHb molecules, which further confirmed the validity of the algorithm.

While the assignment of these two endmembers corresponding to the hemozoin and oxyHb were trivial, the origin of the high intensity signal seen as a "halo" observed just outside the perimeter of the cell [green region in Fig. 5(c)] is not clear. The absorption spectra obtained from the "halo" [see Fig. 5(f)] resembled that of metHb. However, the signal contributing to the halo may be independent of the spectral characteristics of the intracellular components because it is present outside of the cell and its intensity and extension depended on the shape and morphology of the cell. Therefore, it may imply that the spectral signature was associated with the wavelength-dependent scattering as the incoming illumination light was transmitted through and scattered off the cell membrane.

C. Modeling of the Scattering Signal

The diameter of a single erythrocyte is about 7 μm, and the thickness decreases from 2 to 1 μm, from the edge to the center of the bioconcave-shaped cell, suggesting that the Mie scattering theory may be applied to explain the scattering intensity as a function of scattering angle [28]. However, in Mie scattering theory, the scattering intensity of a plane wave illuminating an object with a size comparable or larger than the wavelength of the light is solved at a distance much larger than the wavelength, the so-called far-field zone. Therefore, the interpretation of the scattering involving signal contrast in microscopy using Mie theory is not trivial since the imaging plane in microscopy overlaps with the volume of the scattering object. In microscopy, when a focal volume passes through the field of a scattering object, the collection of this scattered light depends on the spatial position of the focal volume relative to the scatterer, the numerical aperture which determines the range of collection angles, and the

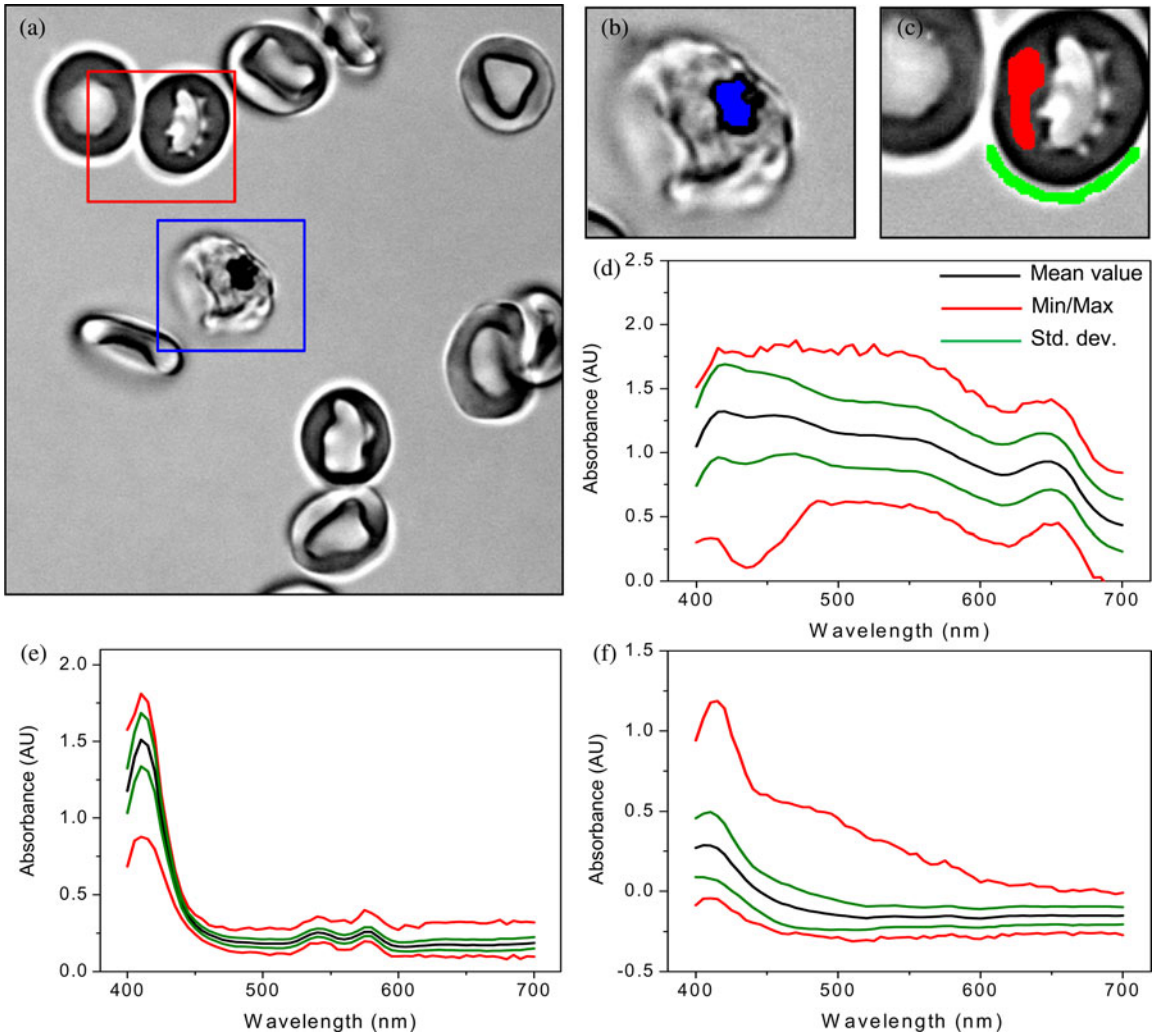

Fig. 5. (a) Averaged intensity map calculated from all the absorption spectra of the mixture of uninfected and *Pf*-infected erythrocytes. An infected cell in the blue box, shown in panel (b), also contains a dark object, a heme crystal formed by malaria parasite inside the cytoplasm. An uninfected cell in the red box, shown in panel (c), also shows typical bioconcave shape and appears dark due to the absorption by hemoglobin present in the cytoplasm. (b) Region of interest (colored in blue) from which several absorption spectra from randomly selected pixel positions within the region are shown in panel (d). (c) Region of interest from which several absorption spectra from randomly selected pixel positions within the red and green regions are shown in panels (e) and (f), respectively.

magnification of the signal onto the detector which determines the solid angle collected by each pixel at the detector.

To estimate the scattering properties of a cell in microscopy data, a simple ray-tracing model of the MiePlot simulation package [29] was applied to a 7-μm diameter sphere of refractive index of 1.41 to mimic the Hb-filled erythrocyte cytoplasm [30]. The model includes the effects of surface reflection, wavelength-dependent absorption of the scattering, and interference between rays. In this model, a beam of light incident upon the surface of the sphere is treated as a bundle of parallel rays that are reflected, absorbed, and/or refracted by the sphere. Treating the incident light at each wavelength as monochromatic coherent light, the intensity of the light scattered in a particular direction depends on the relative amplitudes of each ray and on the phase delay caused by propagation paths through the sphere. The angle of incidence θ_i is defined by

$$\theta_i = 2i - 2\sin^{-1}\left(\frac{\sin i}{n}\right) + (p-1)\cdot 180^\circ \qquad (3)$$

where i is the angle of incidence defined between the field propagating vector and the radial vector from the center to the point of incidence of the ray on the surface, n is the refractive index of the sphere, and $p = 0$, 1, and 2 correspond to external reflection and diffraction off the surface of the sphere, direct transmission through the sphere, and internal reflection within the sphere, respectively.

Fig. 6 shows total scattering intensities of scattering angle versus wavelength for a plane wave transmitting through a 7 μm diameter sphere with the refractive index of 1.41 in a sphere model. Modeling the cell with a curved reflecting surface at the interface between water ($n = 1.33$ at 20 °C) and the cell, the scattering intensities superposed for $p = 0$, 1, and 2 or for $p = 1$ only are calculated and shown in Fig. 6(a) and (b), respectively. The scattering intensity of the incident beam through the sphere (for $p = 1$) may be used to estimate the wavelength-dependent absorption by intracellular Hb. For clarity, Fig. 6(c) displays scattering angle-dependent intensities for several wavelengths

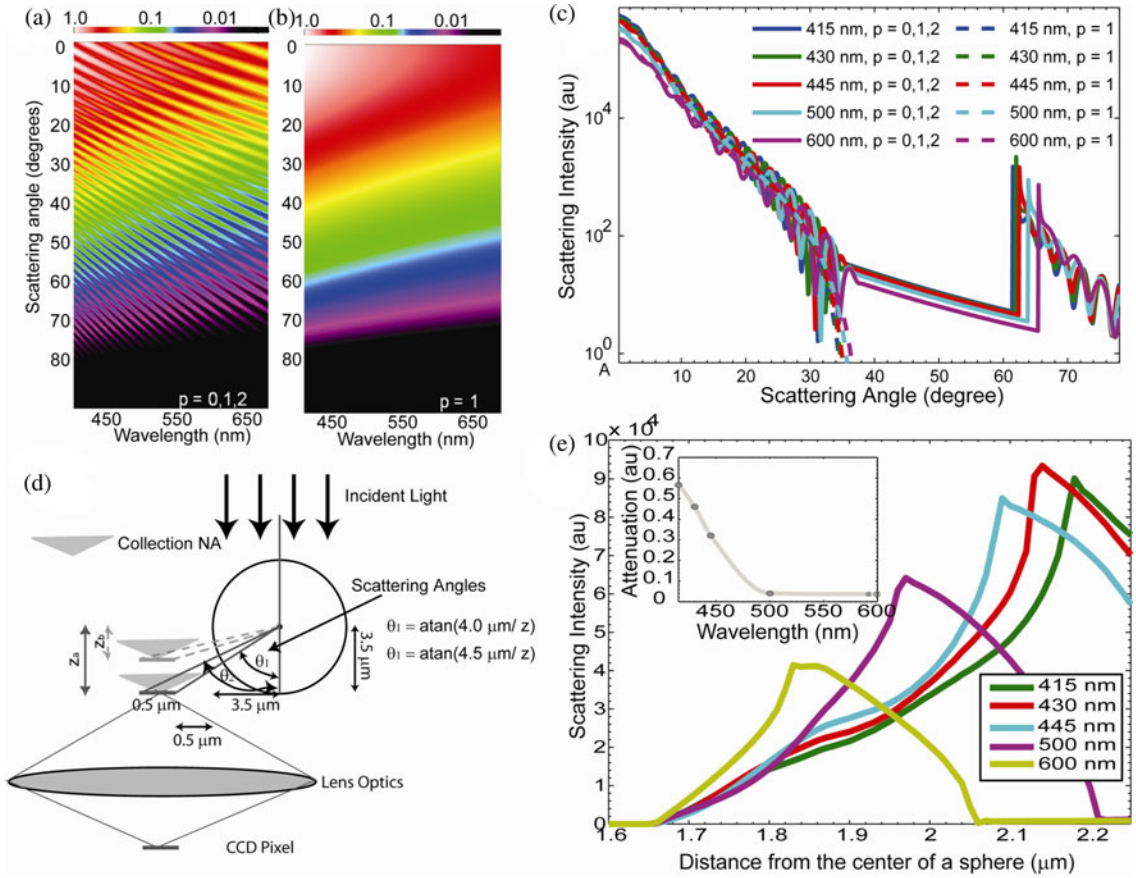

Fig. 6. (a) Total scattering intensity of scattering angle versus wavelength for a plane wave transmitting through a 7 μm diameter sphere with a refractive index of 1.4. Contributions corresponding to external reflection, diffraction, direct transmission, internal reflections up to the second degree are summed. (b) With the same parameters, total scattering intensity of scattering angle versus wavelength, the contribution corresponding to the direct transmission ($p = 1$) through the sphere is calculated. (c) Total scattering intensities versus scattering angle at several different wavelengths. (d) Schematic diagram of the light-collection efficiency according to the position of objective's focal volume. (e) Calculated scattering intensities of light collected by an objective lens at several different wavelengths. The scattering intensity is estimated by integrating the scattering signal falling within the collection solid angle of the objective and is plotted as a function of the position of a focal plane, determined by the distance z from the center of a sphere. The inset shows the data points and the Gaussian fit of the wavelength-dependent attenuation calculated from the scattering intensities for different wavelengths at $z = 1.88$ μm which is a experimentally estimated distance to the focal plane from the center plane of the sphere.

of the incident light superposed for $p = 0$, 1, and 2 or for $p = 1$ only. From these angle-dependent scattering light intensities, the scattering light intensity collected within the focal volume at different sample coordinates was estimated. Fig. 6(d) describes the collection of scattered photons into a light-collecting aperture of a focal volume for an oil immersion objective (NA = 1.4, i.e., angular aperture of 67.5°) that scanned along a vertical line near the edge of the sphere. The effective solid angle within which the scattered photons were collected into the focal volume was defined by the solid angle that overlapped only with the angular aperture of the objective. As the focal volume moves away from the substrate, this effective solid angle decreased, resulting in the decreased intensity of scattered light collected into the focal volume. The collected scattered light intensity as a function of the position of a focal volume aperture at different wavelengths is displayed in Fig. 6(e). In optical microscopy, the depth of field is estimated by

$$d = \frac{\lambda \cdot n}{NA^2} + \frac{n \cdot e}{M \cdot NA} \tag{4}$$

where λ is the wavelength of light, n is the refractive index of the medium (1.515 for oil), NA (1.4) is the objective numerical aperture, e ($\approx$0.3 μm) is the smallest distance that can be resolved by a detector that is placed in the image plane of the objective, and M (60) is the lateral magnification of the objective. Accordingly, $d \approx 0.77 \cdot \lambda = 0.39$ μm for $\lambda = 0.5$ μm. Fig. 6(e) shows that when the focal plane was adjusted within 1.95 μm below the center of the sphere (which is a reasonable approximation for the imaged plane in focus), the collected scattering intensity decreased as λ decreased with a resultant increase in the calculated absorption signal for shorter wavelength light. For instance, the wavelength-dependent scattering intensity at $z = 1.89$ μm showed that the intensities at $\lambda < 500$ nm was smaller than those at longer wavelength to result in calculated absorption spectrum [inset in Fig. 6(e)] which resembled the absorption spectra obtained from the "halo" region seen in Fig. 5(f).

In this study, the absorption by cytoplasmic Hb is not included since the scattered signal for $p = 1$ which corresponds to direct transmission of the light through the sphere falls outside the angular aperture of the objective [see Fig. 6(c)]. However, for

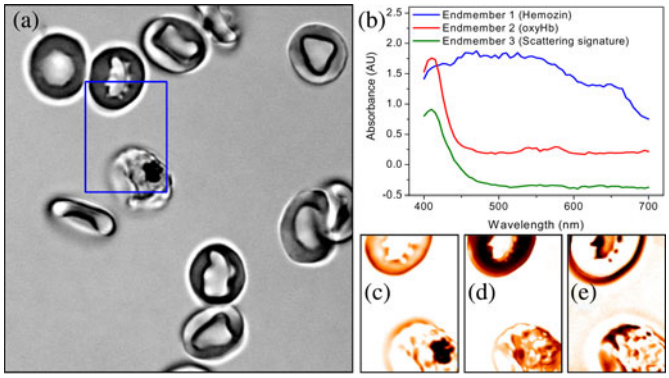

Fig. 7. Endmember extraction and their abundance maps. (a) Averaged intensity map calculated from the data cube of the mixture of uninfected and *Pf*-infected erythrocytes used for the endmember extraction. (b) Three most distinctive endmembers for oxyHb, hemozoin, and membrane scattering were extracted with the SMACC algorithm from regions with known morphological information. Their abundance maps show the localization of each signature spectrum and confirm that the endmember 1, 2, and 3 corresponds to hemozoin, oxyHb, and scattering signature, respectively.

more precise analysis, this sphere model needs to be replaced by a model using a biconcave erythrocyte shape, and the contribution due to wavelength-dependent absorption by intracellular Hb may not be negligible. On the other hand, the sphere model in this study qualitatively describes the contribution of scattering signatures to the hyperspeactral data cube of erythrocytes. Calculation based on biconcave erythrocyte shape is beyond the scope of this study.

D. Automatic Endmember Extraction From Uninfected and Pf-Infected Erythrocytes by the SMACC Algorithm

In the previous section, we extracted each eigenstate endmember for oxyHb, hemozoin, and membrane scattering based on the morphological information. Instead, here we applied the SMACC algorithm to automatically extract the top three dominant endmembers from a data cube of the entire image of mixed uninfected and infected erythrocytes without *a priori* information on the spatial distribution of hemozoin and oxyHb [see Fig. 7(a)]. Fig. 7(b) displays three distinctive endmembers, which are identified by the algorithm. It is noteworthy that the spectral shapes of hemozoin, oxyHb, and scatter-induced absorption are recovered as endmember 1, 2, and 3, respectively, confirming that the SMACC algorithm successfully extracted the key absorption spectral features of major components in uninfected and infected erythrocytes. For further validation, the abundance of each endmember was calculated and is displayed in Fig. 8(c)–(e) using endmember 1, 2, and 3, respectively. Comparing with Fig. 5, each abundance map matches to each sequestered region of hemozoin, oxyHb, or scattering based on *a priori* information on the localized distribution of each component. These results demonstrate the validity of our algorithm to localize the key elements of hemozoin and oxyHb in the mixture of infected and uninfected erythrocytes.

To examine the general utility of our approach, we evaluated the presence and the abundance of these elements in a different image data cube of erythrocytes by applying the previously collected endmembers for hemozoin, oxyHb, and scattering signature [spectra shown in Fig. 7(b)]. Fig. 8(a) shows the averaged intensity image for the data cube. The *Pf*-infected cell is distinguishable from other uninfected cells due to the hemozoin, the crystallized heme formed from digested Hb by parasites. Fig. 8(b) shows that the analysis successfully correlated the hemozoin area that appears as a dark color in the abundance map because the difference in spectral angle of the given area to reference hemozoin spectrum is small. Likewise, other abundance maps clearly showed signatures of oxyHb absorption in uninfected erythrocytes and scattering as indicated by arrows in Fig. 8(c) and (d), respectively.

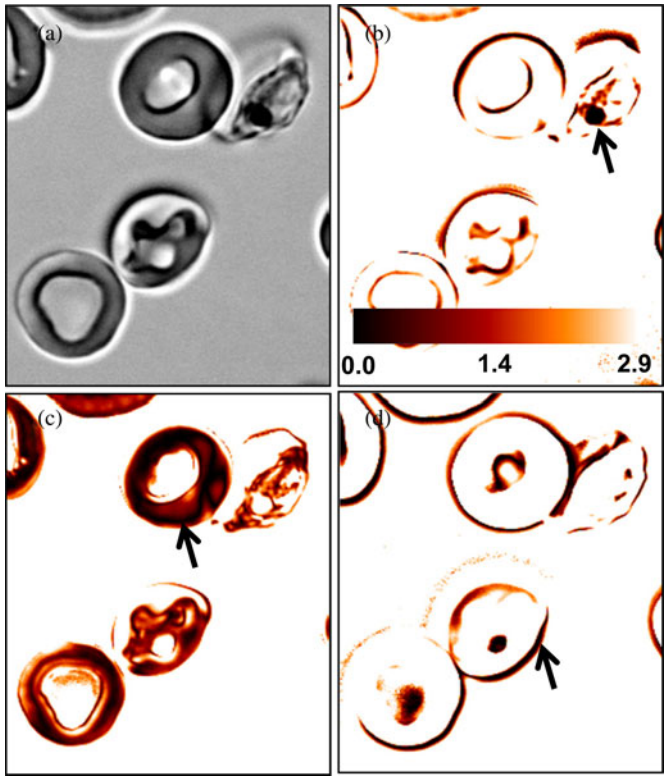

Fig. 8. (a) Bright-field image of erythrocyte sample. A *Pf*-infected cell is located on the top-right corner mixed with uninfected cells. Abundance maps obtained with the endmembers for (b) hemozoin, (c) oxyHb, and (d) scattering signature on a hyperspectral cube of mixed uninfected and infected erythrocytes. The arrows indicate representative areas for each substance.

IV. Conclusion

We have demonstrated the use of a hyperspectral microscope to enable spectroscopic identification of the key biological molecules, oxyHb and hemozoin, in uninfected and *Pf*-infected erythrocytes. The identification of absorption spectra of these endmembers was demonstrated and validated using SMACC endmember extraction and abundance map calculation algorithms applied to the hyperspectral data cube obtained from samples where uninfected and *Pf*-infected erythrocytes coexist. Further application of the hyperspectral imaging and algorithm on a new set of mixed uninfected and *Pf*-infected erythrocytes demonstrates the possibility of image-based pathology to screen single *Pf*-infected cells in human blood sample for the early

detection of malaria infection. This method may be applied to a variety of diagnostics assays to screen blood-borne pathogens at the early stage.

ACKNOWLEDGMENT

The authors would like to thank Dr. D. Samarov, Dr. A. Possolo, Dr. E. Shirley, Dr. Y. J. Lee, and Dr. K. Briggman for useful discussions and valuable comments on this manuscript. This research was performed while J. Y. Lee held a National Research Council Research Associateship Award at NIH (NIBIB)/NIST, and J. F. Lesoine and R. Chang held a National Research Council Research Associateship Award at NIST.

REFERENCES

[1] A. J. Chaudhari, F. Darvas, J. R. Bading, R. A. Moats, P. S. Conti, D. J. Smith, S. R. Cherry, and R. M. Leahy, "Hyperspectral and multispectral bioluminescence optical tomography for small animal imaging," *Phys. Med. Biol.*, vol. 50, pp. 5421–5441, Dec. 2005.

[2] B. S. Sorg, B. J. Moeller, O. Donovan, Y. T. Cao, and M. W. Dewhirst, "Hyperspectral imaging of hemoglobin saturation in tumor microvasculature and tumor hypoxia development," *J. Biomed. Opt.*, vol. 10, no. 4, p. 44004, Jul./Aug. 2005.

[3] M. E. Martin, M. B. Wabuyele, K. Chen, P. Kasili, M. Panjehpour, M. Phan, B. Overholt, G. Cunningham, D. Wilson, R. C. DeNovo, and T. Vo-Dinh, "Development of an advanced hyperspectral imaging (HSI) system with applications for cancer detection," *Ann. Biomed. Eng.*, vol. 34, pp. 1061–1068, Jun. 2006.

[4] G. Zavattini, S. Vecchi, G. Mitchell, U. Weisser, R. M. Leahy, B. J. Pichler, D. J. Smith, and S. R. Cherry, "A hyperspectral fluorescence system for 3D in vivo optical imaging," *Phys. Med. Biol.*, vol. 51, pp. 2029–2043, Apr. 21 2006.

[5] R. M. Levenson, P. J. Cronin, and N. R. Harvey, "Spectral imaging and biomedicine: New devices, new approaches," in *Proc. 31st Appl. Imagery Pattern Recog. Workshop*, Oct. 2002, pp. 105–111.

[6] K. J. Zuzak, M. D. Schaeberle, E. N. Lewis, and I. W. Levin, "Visible reflectance hyperspectral imaging: Characterization of a noninvasive, in vivo system for determining tissue perfusion," *Analyt. Chem.*, vol. 74, pp. 2021–2028, May 2002.

[7] L. T. Nieman, M. B. Sinclair, J. A. Timlin, H. D. T. Jones, and D. M. Haaland, "Hyperspectral imaging system for quantitative identification and discrimination of fluorescent labels in the presence of autofluorescence," in *Proc. 3rd IEEE Int. Symp. Biomed. Imaging: Nano Macro*, Apr. 2006, vol. 1-3, pp. 1288–1291, 1391.

[8] Z. Y. Liu, S. H. Ma, Y. H. Ji, L. Liu, Z. X. Hu, J. H. Guo, H. Ma, and Y. H. He, "Quasi-confocal, multichannel parallel scan hyperspectral fluorescence imaging method optimized for analysis of multicolor microarrays," *Analyt. Chem.*, vol. 82, pp. 7752–7757, Sep. 2010.

[9] M. Miljkovic, T. Chernenko, M. J. Romeo, B. Bird, C. Matthaus, and M. Diem, "Label-free imaging of human cells: Algorithms for image reconstruction of Raman hyperspectral datasets," *Analyst*, vol. 135, pp. 2002–2013, 2010.

[10] J. T. Zoueu, G. L. Loum, T. C. Haba, M. Brydegaard, and H. Menan, "Optical microscope based on multispectral imaging applied to plasmodium diagnosis," *J. Appl. Sci.*, vol. 8, pp. 2711–2717, 2008.

[11] O. Carrasco, R. Gomez, A. Chainani, and W. Roper, "Hyperspectral imaging applied to medical diagnoses and food safety," in *Proc. Geo-Spatial and Temporal Image and Data Exploitation III*, 2003, vol. 5097, pp. 215–221, 2003.

[12] N. J. Crane, Z. D. Schultz, and I. W. Levin, "Contrast enhancement for in vivo visible reflectance imaging of tissue oxygenation," *Appl. Spectroscopy*, vol. 61, pp. 797–803, Aug. 2007.

[13] G. M. Palmer, A. N. Fontanella, G. Q. Zhang, G. Hanna, C. L. Fraser, and M. W. Dewhirst, "Optical imaging of tumor hypoxia dynamics," *J. Biomed. Opt.*, vol. 15, p. 066021, Nov./Dec. 2010.

[14] A. Nouvong, B. Davis, B. Hoogwerf, A. Tajaddini, E. Mohler, and E. Medenilla, "Evaluation of diabetic foot ulcer healing with hyperspectral imaging of oxyhemoglobin and deoxyhemoglobin," *Diabetes Care*, vol. 32, pp. 2056–2061, Nov. 2009.

[15] C. C. Winterbourn, "Reactions of superoxide with hemoglobin," in *CRC Handbook Method Oxygen Radical Research*. Boca Raton, FL: CRC Press, 1985, pp. 137–141.

[16] E. R. Jaffe and H. S. Hsieh, "DPNH-methemoglobin reductase deficiency and hereditary methemoglobinemia," *Semin. Hematology*, vol. 8, pp. 417–437, 1971.

[17] C. D. Fitch and P. Kanjananggulpan, "The state of ferriprotoporphyrin IX in malaria pigment," *J. Biol. Chem.*, vol. 262, pp. 15552–15555, Nov. 1987.

[18] S. Pagola, P. W. Stephens, D. S. Bohle, A. D. Kosar, and S. K. Madsen, "The structure of malaria pigment beta-haematin," *Nature*, vol. 404, pp. 307–310, Mar. 2000.

[19] E. Hempelmann, "Hemozoin biocrystallization in Plasmodium falciparum and the antimalarial activity of crystallization inhibitors," *Parasitol. Res.*, vol. 100, pp. 671–676, Mar. 2007.

[20] B. R. Wood, S. J. Langford, B. M. Cooke, F. K. Glenister, J. Lim, and D. McNaughton, "Raman imaging of hemozoin within the food vacuole of Plasmodium falciparum trophozoites," *FEBS Lett.*, vol. 554, pp. 247–252, Nov. 2003.

[21] G. Ostera, F. Tokumasu, C. Teixeira, N. Collin, J. Sa, J. Hume, S. Kumar, J. Ribeiro, G. S. Lukat-Rodgers, and K. R. Rodgers, "Plasmodium falciparum: Nitric oxide modulates heme speciation in isolated food vacuoles," *Exp. Parasitol.*, vol. 127, pp. 1–8, Jan. 2011.

[22] J. Gruninger, A. J. Ratkowski, and M. L. Hoke, "The sequential maximum angle convex cone (SMACC) endmember model," in *Proc. Algorithms Technol. Multispectral, Hyperspectral, Ultraspectral Imagery X*, 2004, vol. 5425, pp. 1–14.

[23] J. H. Gruninger, A. J. Ratkowski, and M. L. Hoke, "The extension of endmember extraction to multispectral scenes," in *Proc. Algorithms Technol. Multispectral, Hyperspectral, Ultraspectral Imagery X*, 2004, vol. 5425, pp. 15–30.

[24] M. L. Clarke, M. Litorja, D. W. Allen, D. V. Samarov, and J. Hwang, "Characterization of hyperspectral imaging and analysis via microarray printing of dyes," *Proc. SPIE*, vol. 7891, p. doi:10.1117/12.875521, 2011.

[25] F. Tokumasu, R. M. Fairhurst, G. R. Ostera, N. J. Brittain, J. Hwang, T. E. Wellems, and J. A. Dvorak, "Band 3 modifications in Plasmodium falciparum-infected AA and CC erythrocytes assayed by autocorrelation analysis using quantum dots," *J. Cell Sci.*, vol. 118, pp. 1091–1098, Mar. 2005.

[26] F. Tokumasu, G. A. Nardone, G. R. Ostera, R. M. Fairhurst, S. D. Beaudry, E. Hayakawa, and J. A. Dvorak, "Altered membrane structure and surface potential in homozygous hemoglobin C erythrocytes," *PLoS One*, vol. 4, p. e5828, Jun. 2009.

[27] A. U. Orjih and C. D. Fitch, "Hemozoin production by Plasmodium falciparum: Variation with strain and exposure to chloroquine," *Biochim. Biophys. Acta*, vol. 1157, pp. 270–274, Jul. 1993.

[28] V. V. Barun and A. P. Ivanov, "Localized light absorption by hemoglobins of an erythrocyte suspension," *J. Appl. Spectroscopy*, vol. 76, pp. 487–496, Jul. 2009.

[29] C. F. Bohren and D. R. Huffman, *Absorption and Scattering of Light by Small Particles*. Hoboken, NJ: Wiley-Interscience, 1983, pp. 83–129.

[30] Y. K. Park, M. Diez-Silva, G. Popescu, G. Lykotrafitis, W. S. Choi, M. S. Feld, and S. Suresh, "Refractive index maps and membrane dynamics of human red blood cells parasitized by Plasmodium falciparum," *Proc. Natl. Acad. Sci. USA*, vol. 105, pp. 13730–13735, Sep. 2008.

Ji Youn Lee received the B.S., M.S., and Ph.D. degrees in chemical engineering from the Seoul National University, Seoul, Korea.

She is a National Research Council Postdoctoral Research Associate with a joint appointment at National Institute of Standards and Technology (NIST), MD, and National Institutes of Health, MD. Her research at NIST/NIH focuses on label-free optical imaging, which involves hyperspectral imaging (either wide-field or confocal) for biomedical applications. Before joining NIST, she was a Postdoctoral Researcher at the University of California, Davis, where she was involved in developing miniaturized cell cultures with diverse microscale techniques, such as microarraying, microfabrication, surface engineering, with biomaterials.

Matthew L. Clarke received the B.S. degree in chemistry from the University of Wisconsin-Green Bay, WI, and the M.S. and Ph.D. degrees in analytical chemistry from the University of Michigan, Ann Arbor.

He was with National Institute of Standards and Technology, MD, as a National Research Council Postdoctoral Fellow and as a Guest Researcher from 2006 to 2010. His research at NIST focused on multimodal optical imaging and image processing, particularly related to biomedical imaging and assays and nanoparticle metrology. He is currently with the National Gallery of Art, Washington, DC, where he is involved in photographic materials research related to conservation.

Fuyuki Tokumasu received the B.S. degree in physics from Birmingham-Southern College, Birmingham, AL, the M.S. degree in biophysics from The Ohio State University, Columbus, OH, and the Ph.D. degree in human and environmental studies from Kyoto University, Kyoto, Japan.

He is a Staff Scientist at the Laboratory of Malaria and Vector Research, National Institutes of Health (NIH), MD. His Ph.D. and early work at NIH involved nanoscale molecular interactions in biomembrane using atomic force microscopy. He is currently focusing on membrane modifications by *Pf* parasite using high-resolution microscopy and fluorescence life-time microscopy.

John F. Lesoine received the B.S. degree in physics from Moravian College, Bethlehem, PA, and the Ph.D. degree in optics from the University of Rochester, Rochester, NY. His Ph.D. research involved the development of single molecule recycling (SMR) and single molecule data analysis methods. SMR is a nanofluidic technique used to repeatedly measure the same biomolecule without surface tethering.

He is an American Recovery and Reinvestment Act National Research Council Postdoctoral Research Associate at the Physical Measurement Laboratory, National Institute of Standards and Technology (NIST), MD, where he is involved in research related to single-molecule imaging techniques and polarimetric imaging techniques for the label-free discrimination of different biomarkers and cell types.

David W. Allen received the B.A. degree in chemistry and the M.S. degree in environmental biology from Hood College, Frederick, MD and completing his dissertation for a Ph.D. degree in earth systems and geoinformation sciences with a concentration in remote sensing from George Mason University, Fairfax, VA, in 2011.

He is currently with National Institute of Standards and Technology (NIST), MD, for more than 14 years. Prior to joining NIST, he worked for several electronic manufacturing companies. His research interests include the optical properties of materials, spectral signatures, and hyperspectral imaging for the environment, defense, and medicine.

Robert Chang received the B.S. degree in chemical engineering from The University of Pennsylvania, Philadelphia, PA, and the Ph.D. degree in mechanical engineering from Drexel University, Philadelphia, PA. His Ph.D. research involved the development of biofabrication systems to create reproducible, high-fidelity 3-D microorgans for high-throughput *in vitro* drug toxicological screening.

He is a National Research Council Postdoctoral Research Associate at the Physical Measurement Laboratory, National Institute of Standards and Technology (NIST), MD, where he has been involved in developing novel optical phantom approaches for the characterization and calibration of various optical modalities including optical coherent tomography and confocal microscopy for axial resolution and contrast as well as an oximetric phantom testbed for hyperspectral imaging of oxygen saturation levels for wound healing applications and surgical scenes.

Maritoni Litorja received the Ph.D. degree in physical/analytical chemistry from Northwestern University, IL, where her research focused on investigating the phenomenon of adsorbate Raman signal enhancement by small metal particles in ultrahigh vacuum.

She joined National Institute of Standards and Technology (NIST), MD, as a National Research Council Postdoctoral Fellow in the Surface and Microanalysis Division, where she was involved in research on oxygen radicals on surfaces. She is currently a Research Chemist at the Optical Technology Division, NIST. Prior to NIST, she worked in industry as an analytical chemist and with the Molecular Dynamics group at Argonne National Laboratories studying radicals and other transients relevant to combustion and atmospheric chemistry. Her current research interests include 1) designing standard analytical chemistry methodology to validate *in situ* measurement methods applied to problems where separations chemistry is not possible, such as in *in vivo* spectroscopic imaging, and 2) application of photogrammetric techniques for image-based dimensional metrology.

Jeeseong Hwang received the B.S. degree in physics from the Seoul National University, Seoul, Korea, and the Ph.D. degree in condensed matter physics from Michigan State University, East Lansing. His Ph.D. thesis was on scanning probe microscopy of nanoscale quantum structures and metal surfaces.

His work at the National Institute of Standards and Technology (NIST), MD, in 1994 began with an award of the U.S. National Research Council Fellowship on near-field optical scanning probe microscopy of nanoscale biomimetic and biological materials and structures. He is currently a Project Leader and Research Biophysicist in the Physical Measurement Laboratory of NIST of the U.S. Department of Commerce. Before joining NIST, he was a Research Scientist in Immunology Laboratory, Biology Department, Johns Hopkins University, where he investigates biophysical aspects of immune response of human cells using superresolution near-field scanning optical microscopy and other laser-based optical imaging techniques in collaboration with AT&T Bell Laboratories. His current research interests include nanobiophotonics for quantitative biophysics and nanomedicine, involving development and application of the following areas: multimodal molecular imaging techniques; integrated optical analysis platforms for multiplexed bioassays; bioinspired assembly of nanoscale building blocks for optical biosensors; and quantitative image analysis software for multiplexed dynamic bioassays.

Dr. Hwang's recent contributions to professional societies include Program Committee of the Annual SPIE BiOS Convention since 2006, ISO Scanning Probe Microscopy Subcommittee in 2005–2007. He received many awards including the US/DoC Silver Medal in 2008. He also leads the NIST Innovations in Measurement Science Program on Optical Medical Imaging.